



Technical Note

Mapping Coastal Wetlands and Their Dynamics in the Yellow River Delta over Last Three Decades: Based on a Spectral Endmember Space

Kun Tan ^{1,2}, Danfeng Sun ¹, Wenjun Dou ³, Bin Wang ³, Qiangqiang Sun ¹, Xiaojie Liu ⁴, Haiyan Zhang ⁴, Yang Lan ⁵ and Fei Lun ^{1,2,*}

¹ College of Land Science and Technology, China Agricultural University, Beijing 100193, China; b20203210944@cau.edu.cn (K.T.); sundf@cau.edu.cn (D.S.); qiangsun@cau.edu.cn (Q.S.)

² Key Laboratory of Southeast Coast Marine Information Intelligent Perception and Application, Ministry of Natural Resources, Zhangzhou 363000, China

³ Yantai Geological Survey Center of Coastal Zone, China Geological Survey, Yantai 264000, China; douwenjun@mail.cgs.gov.cn (W.D.); wbing@mail.cgs.gov.cn (B.W.)

⁴ Key Laboratory of Natural Resource Coupling Process and Effects, Institute of Geographic Sciences and Natural Resources Research, Chinese Academy of Sciences, Beijing 100101, China; liuxj@igsrr.ac.cn (X.L.); zhanghaiyan823@163.com (H.Z.)

⁵ The Bartlett School of Environment, Energy and Resources, University College London, London WC1E 6BT, UK; ucbq737@ucl.ac.uk

* Correspondence: lunfei@cau.edu.cn

Abstract: The accurate mapping and analysis of coastal wetlands and their dynamics are crucial for local coastal wetland protection, sustainable social development, and biodiversity preservation. However, detailed mapping and comprehensive analysis of coastal wetlands remain scarce. In this study, we utilized Landsat-TM/OLI remote sensing data and employed the linear spectral mixture analysis (LSMA) method to map changes in coastal wetlands and analyze their dynamics in the Yellow River Delta (YRD) from 1991 to 2020. Our mapping results demonstrate high accuracy and are consistent with previous studies, boasting an overall accuracy exceeding 96%. During the period of 1991–2020, the YRD estuary expanded by approximately 8744.58 ha towards the east and north. The vegetation of *P. australis* and *S. salsa* underwent transformation due to agricultural practices or degradation to bare flats. Moreover, these areas saw extensive colonization by the invasive species *S. alterniflora*. Over the three decades, *S. alterniflora* expanded approximately 5 km along the coast, significantly impacting the local coastal wetland biodiversity. Furthermore, a considerable number of natural wetlands transitioned into human-made wetlands from 1991 to 2014. In particular, bare flats underwent substantial changes, transforming into aquaculture sites and salt exploitation areas. These dynamics in coastal wetlands had significant repercussions on local ecosystems, including wetland fragmentation, biodiversity depletion, and water pollution. However, post-2014, numerous wetland protection strategies were implemented, resulting in the restoration of natural wetlands. Detailed wetland mapping and dynamic analysis furnish valuable insights for the management, protection, and sustainable utilization of diverse coastal wetlands.

Keywords: coastal wetland mapping; dynamic analysis; endmembers (EMs); linear spectral mixture analysis (LSMA); the Yellow River Delta (YRD)



Citation: Tan, K.; Sun, D.; Dou, W.; Wang, B.; Sun, Q.; Liu, X.; Zhang, H.; Lan, Y.; Lun, F. Mapping Coastal Wetlands and Their Dynamics in the Yellow River Delta over Last Three Decades: Based on a Spectral Endmember Space. *Remote Sens.* **2023**, *15*, 5003. <https://doi.org/10.3390/rs15205003>

Academic Editor: Frédéric Frappart

Received: 5 September 2023

Revised: 10 October 2023

Accepted: 16 October 2023

Published: 18 October 2023



Copyright: © 2023 by the authors. Licensee MDPI, Basel, Switzerland. This article is an open access article distributed under the terms and conditions of the Creative Commons Attribution (CC BY) license (<https://creativecommons.org/licenses/by/4.0/>).

1. Introduction

Coastal wetlands, acting as natural transition zones between land and sea, play a vital role in providing crucial ecological services [1–3], encompassing biodiversity maintenance, carbon sequestration, soil and water control, among other essential, ecosystem services [4,5]. However, due to climate change, natural disturbances, and human activities, coastal wetlands are currently facing significant challenges globally, such as wetland vegetation

degradation, biodiversity losses, and environment pollution, putting coastal wetlands at risk of degradation or disappearance [6–8]. The Ramsar Convention categorizes coastal wetlands into two types: natural coastal wetlands and human-made coastal wetlands. The former includes shallow seas, estuary waters, tidal flats, salt marshes, and lakes, while the latter includes aquaculture areas, salt exploitation sites, reservoirs, and paddy fields. The invasive species of *S. alterniflora* extensively displaced the native *S. salsa* habitat in the Yancheng National Nature Reserve, resulting in local biodiversity losses [9]. Tidal flats, despite being habitats for many species, offer limited direct economic benefits and were extensively exploited for aquaculture in the YRD during the period of 1984–2018 [10]. Coastal land reclamation cumulatively contributed to about 22% of land resources for aquaculture over the past 30 years [11]. Therefore, accurate mapping of coastal wetland dynamics is of paramount importance for local environmental protection and sustainable social development [12].

Traditional field surveys face significant challenges in monitoring coastal wetland dynamics over a long term and across large areas [13]. Leveraging its wide coverage and open access, remote sensing data offer real-time dynamic monitoring capabilities over extensive regions and is extensively utilized for coastal wetland mapping [14,15]. Notably, with Landsat images, Wang et al. (2020) mapped Chinese coastal wetlands in 2018, including various types, such as evergreen, deciduous, and tidal flats [16]; Sun et al. (2020) mapped coastal wetlands in the Bohai Rim by the random forest model, including wetland and water, non-wetland vegetation, and non-vegetated land [17]. While these studies provided valuable insights into coastal wetland monitoring and conservation, they often lack detailed information on wetland dynamics, including wetland vegetation changes, biological invasions, expansion of human-made wetlands, and more. Therefore, it is crucial to explore coastal wetland dynamics with high spatiotemporal heterogeneity, employing detailed coastal wetland classification. The linear spectral mixture analysis (LSMA) method, utilizing spectral endmembers (EMs), enables physics-based standardized quantification of fractional abundance. This technique proved to be highly effective in detailed land cover mapping and dynamic analysis [18,19]. By using multi-seasonal images and incorporating EMs, LSMA can capture phenological information of different land covers, providing accurate classification results even with limited samples [20]. Given challenges such as poor accessibility to certain areas and complex conditions related to periodic tides, LSMA stands out as an advantageous method to map coastal wetland dynamics [21,22].

The Yellow River Delta (YRD) is situated at a critical convergence point among mainland, river, and sea, boasting an extensive area of natural coastal wetlands. These natural coastal wetlands play a vital role in the local ecosystems and are instrumental for social development. However, they are highly sensitive and vulnerable to climate change and human disturbances, posing significant challenges and garnering widespread attention [17,23,24]. Concurrently, the rapid expansion of aquaculture and salt exploitation sites introduced significant problems, including water pollution, wetland degradation, and biodiversity losses. Given these challenges, it is urgent to comprehensively explore the dynamics of coastal wetlands in the YRD.

Therefore, we employed Landsat-TM/OLI remote sensing data and utilized the LSMA method to map changes in coastal wetlands. Our objective was to conduct a dynamic analysis to aid in the local protection, management, and sustainable utilization of coastal wetlands. The specific objectives included: (1) mapping the spatiotemporal changes of coastal wetlands in the YRD from 1991 to 2020 using the LSMA method, according to our detailed classification framework; (2) exploring their dynamics and interactions of natural and human-made coastal wetlands in the YRD over these 30 years from temporal, spatial, and landscape perspectives; and (3) discussing the impacts of detailed coastal wetland dynamics in the YRD and providing valuable insights for managing, protecting, and utilizing diverse coastal wetlands, assisting in making informed decisions regarding their trade-offs.

2. Materials

2.1. Study Area

Our study area of YRD is located in Dongying City, Shandong Province and in the southwest area of the Bohai Sea ($118^{\circ}07'0''$ – $119^{\circ}19'20''$ E, $36^{\circ}55'0''$ – $38^{\circ}10'0''$ N), with abundant coastal wetlands there (Figure 1). The YRD is characterized with a warm temperate continental monsoon climate, with the annual mean temperature of 12.1 – 12.6 °C and the annual rainfall of 550 mm. The tides are irregular semidiurnal with an average sea-level change of 141 cm. Our study area presents flat terrain but complex geological conditions, and local soil types are dominated by tidal soils and saline soils. Local land use is strongly affected by the salinization process [25,26], especially in the YRD estuary. The native species of *P. australis* and *S. salsa*, and the invasive species of *S. alterniflora* are three typical forms of wetland vegetation there.

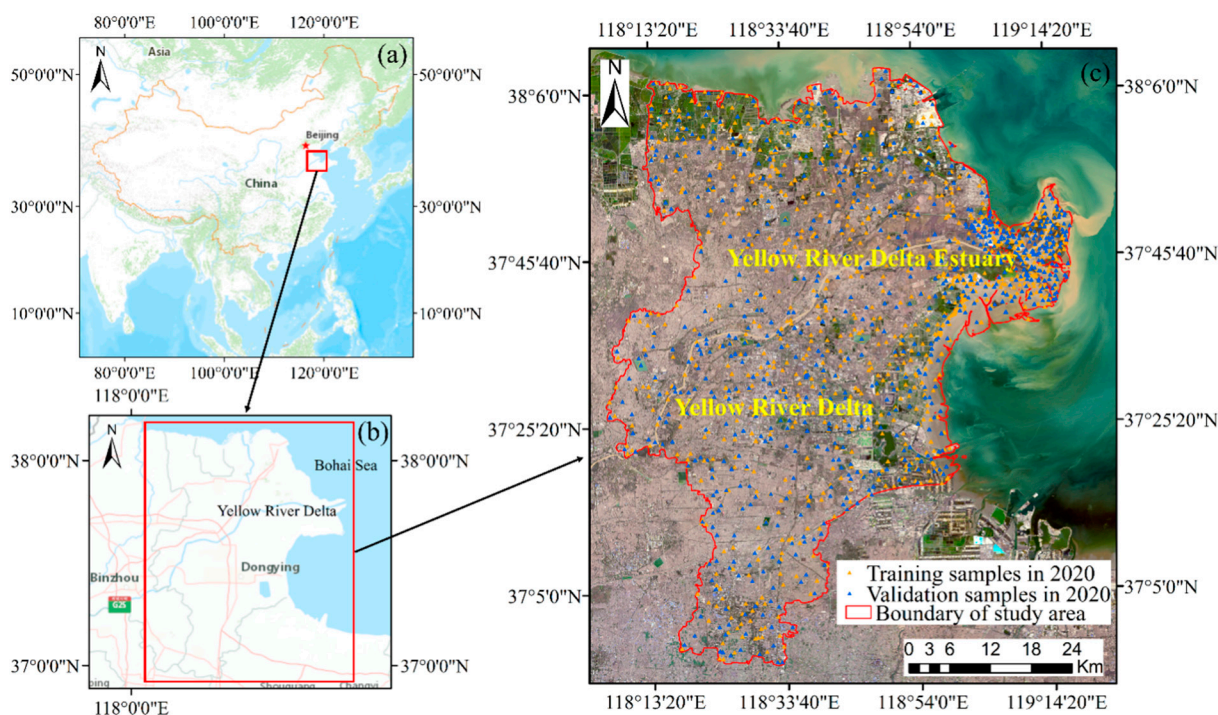


Figure 1. The location of our study area. (a) China, (b) Bohai Sea and YRD, (c) true color composites of red, green and blue bands (Landsat-8 OLI).

The YRD is the youngest wetland ecosystem in China, but it plays an important role in global climate change, biodiversity conservation, and wetland conservation [27,28]. Furthermore, Dongying City was listed as one of international wetland cities in 2018. With high sediment-laden content, the Yellow River transports a large amount of sediment to the estuary each year. The Yellow River and tidal movements have great influences on regional hydrological processes and the evolution of coastal wetlands. In recent years, intensive natural and human disturbance changed local coastal wetlands dynamics (such as natural coastal wetland losses, human-made wetland, and invasive species expansion), which greatly impacted local coastal ecosystem and social development.

2.2. Data Sources and Pre-Processing

2.2.1. Remote Sensing Data

The remote sensing data of Landsat-5 TM and Landsat-8 OLI were derived from the Landsat Collection 2 Level-2 Science Products (<https://earthexplorer.usgs.gov/>, (accessed on 20 June 2022)), which was uniformly preprocessed. A total of 19 Landsat TM/OLI images covered our study area, including two image scenes (path 121, row 034 and path 121, row 035) (detailed see the Table S1). The spatial resolution of all images is 30 m. It

is hard to obtain high-quality images in coastal areas, and thus some images in different years for coastal wetland mapping for the same year. Furthermore, the ENVI 5.3.1 software was used for image cropping to obtain surface reflectance data in our study area.

2.2.2. Training and Validation Samples

Training and validation sample data were obtained based on field surveys, Google Earth, Landsat satellite images, and published literature (detailed see the Table S2). Hand-held GPS was used to locate coastal wetlands during field surveys, and their distribution was also recorded and photographed. A total of 687 sample points were included by field survey in different years. Among them, 328 field samples were provided by the Yellow River Estuary Land–Sea Interaction Field Research Station. Furthermore, we also conducted interviews to understand the historical information and spatial distribution of different coastal wetlands, as well as to local landscape and classification knowledge.

3. Methods

We developed a novel detailed coastal wetland classification framework using Landsat images in a multi-seasonal spectral EM space (Figure 2). Initially, we employed principal component (PC) transformation on multi-seasonal remote sensing images to identify dimensions of the spectral mixing space and define spectral EMs. Subsequently, considering the seasonal variation in different EMs, we determined the purest pixel using the vertex of the polygonal scatter diagram, calculating the average reflectance of the EM pixel as the standard EM spectrum. Following this, a fully constrained LSMA model was applied using the four-EM standard spectral library to acquire spectral EM fraction images. Lastly, utilizing the multi-seasonal spectral EM fraction images, we employed the random forest (RF) model to map detailed coastal wetlands spanning from 1991 to 2020.

3.1. Coastal Wetland Classification System

We defined a comprehensive coastal wetland classification system for the Yellow River Delta (YRD) based on guidelines from the Ramsar Convention and China’s National Standard of Wetland Classification (GB/T 24708-2009 [29]). This system took into account the unique hydrological, soil, and biological conditions specific to the YRD (Table 1). Coastal wetlands in the YRD were categorized into two main types: natural wetlands and human-made wetlands. Natural wetlands encompassed wetland vegetation (*S. alterniflora*, *P. australis*, and *S. salsa*), tidal flats (bare flat and wet tidal flat), as well as river and lake areas. On the other hand, human-made wetlands included aquaculture, salt exploitation sites, reservoirs, and paddy fields. Additionally, we identified two non-wetland categories: arable land and built-up areas.

3.2. The Methods of Coastal Wetland Mapping

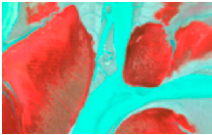
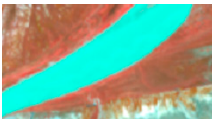
3.2.1. Linear Spectral Mixture Analysis (LSMA)

The accurate identification of decomposable spectral endmember (EM) types is crucial for linear spectral mixture analysis (LSMA) [30]. In this study, we utilized the principal component (PC) transformation of multi-seasonal remote sensing images to determine the dimensions of the spectral mixing space and identify the number and type of spectral EMs [30–32]. The first three principal components of remote sensing images contributed more than 98% (Figure S1), indicating that the intrinsic dimension of the spectral space was three [31]. Hence, we selected four standard EMs in this study (the number of endmembers is generally one more than the intrinsic dimensionality of the spectral space): bare soil (SL), saline (SA), green vegetation (GV), and dark surface (DA, including water and shadow). The LSMA method is defined as follows:

$$R_{i,j} = \sum_{k=1}^n F_{i,k} E_{k,j} + \varepsilon_{i,j} \quad (1)$$

where $R_{i,j}$ is the spectral reflectance of the i^{th} pixel at the band j , n is the total number of endmembers, $F_{i,k}$ is the fraction of the k^{th} endmember in the i^{th} pixel, $E_{k,j}$ represents the spectral reflectance of the k^{th} endmember in the j^{th} band. $\varepsilon_{i,j}$ is the residual error of the LSMA model.

Table 1. The coastal wetland classification system in our study.

Category I	Category II	Category III	Description	Landsat-8 OLI Image Example	Field Photo Example
Natural wetlands	Wetland vegetation	<i>S. alterniflora</i>	<i>S. alterniflora</i> mainly grows in the middle and low tide areas, with its growing season from April to October.		
		<i>P. australis</i>	<i>P. australis</i> is mainly distributed in the riverbanks, with its growing season from April to October.		
		<i>S. salsa</i>	<i>S. salsa</i> is mainly distributed in mid-tide or high-tide area with various coverage, with its growing season of May to November.		
	Tidal flats	Bare flat	Bare flat is located in the mid-tide to high-tide area, with lower water content but higher soil salinization than wet tidal flat.		
		Wet tidal flat	Wet tidal flat is located in the low tide area, has no vegetation cover, and is periodically immersed in water.		
		Rivers and lakes	Permanent or intermittent riverine and lacustrine wetland.		
Human-made wetlands	Aquaculture	Artificial wetlands for fish/shrimp/crab/sea cucumber farming.			
	Salt exploitation sites	Artificial wetlands for salt production.			
	Reservoirs	Artificial wetlands for water storage.			
	Paddy field	Paddy fields are mainly distributed near rivers and villages, and the single-season rice is grown in our study area.			

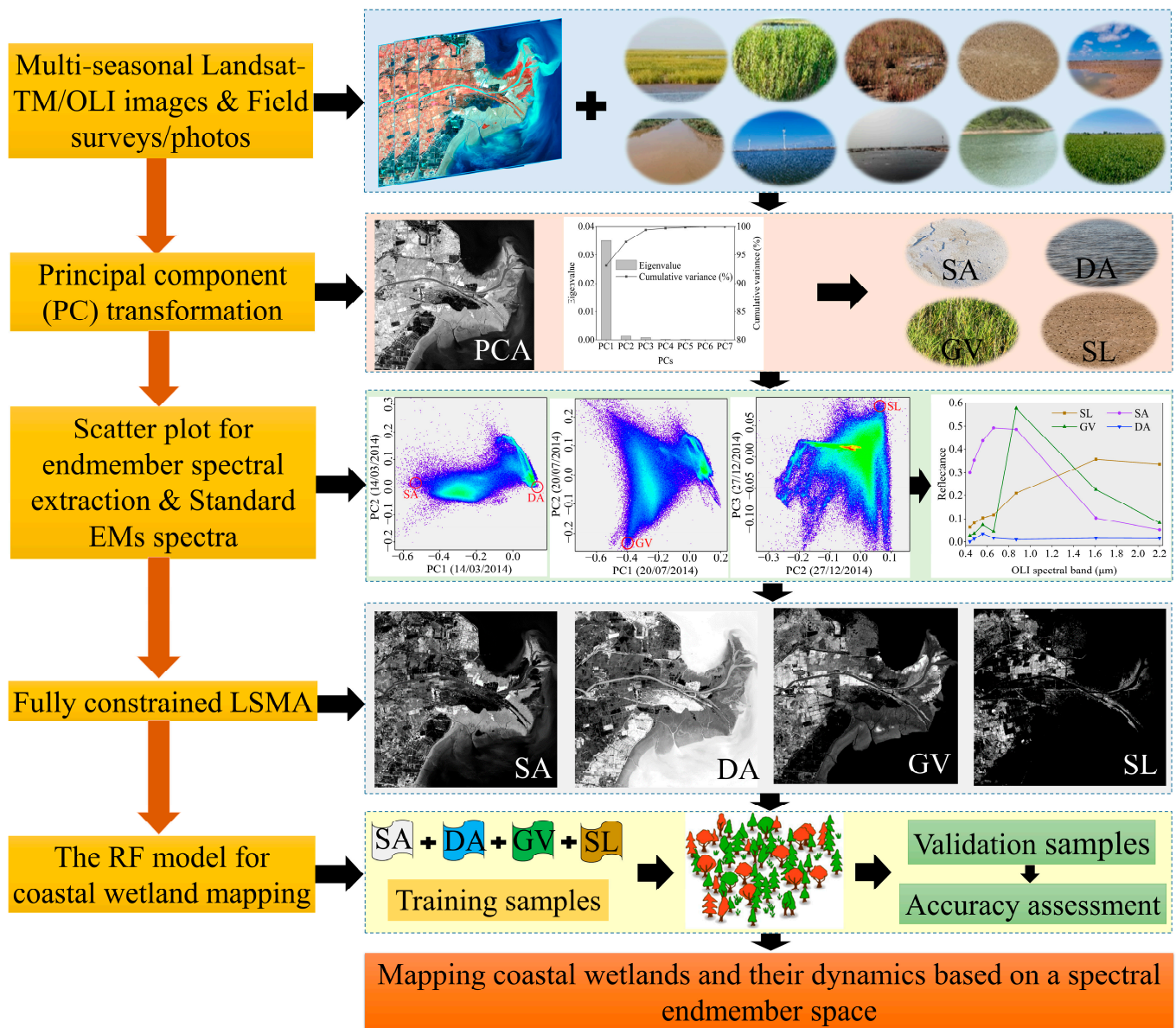


Figure 2. The new detailed coastal wetland classification framework based on EMs space.

The endmembers (EMs) of DA and SA exhibit high purity in spring or early summer, while the EMs of GV and SL can be obtained in summer and winter (or autumn) due to their seasonal variation. Consequently, using the principal component (PC) transformation of Landsat-5 TM images, DA and SA in June 1999, GV in August 1999, and SL in November 2000 were chosen to run the LSMA model for mapping in 1991, 2000, and 2008. Similarly, based on the PC transformation of Landsat-8 OLI images, DA and SA in March 2014, GV in July 2014, and SL in December 2014 were selected for the LSMA models in 2014 and 2020. The selected EMs were derived from the vertices of the scatter plots (Figures S2 and S3). To ensure stability and variability of the EMs in our study area, we selected 200 to 400 pixels for each EM, and the average reflectance of these pixels was calculated as the standard EM spectrum (Figure 3).

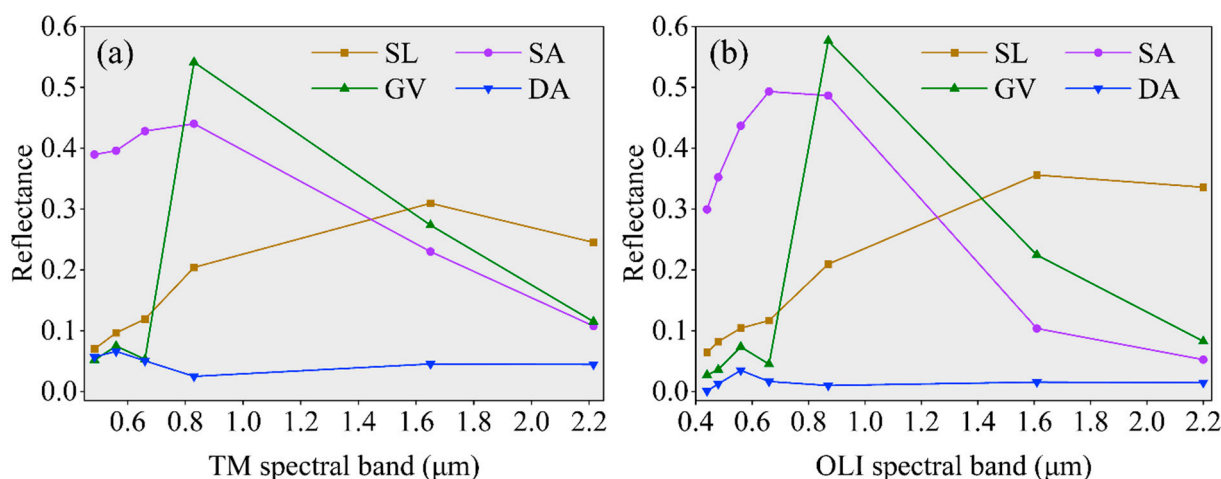


Figure 3. The standard spectra of four EMs, including bare soil (SL), saline (SA), green vegetation (GV), and dark surfaces (DA). (a) the standard spectra of Landsat-5 TM, (b) the standard spectra of Landsat-8 OLI.

The LSMA model was demonstrated to effectively analyze the spatiotemporal variation between spectral EMs [20,32]. In our study, a fully-constrained LSMA model utilizing four EMs (SL, SA, GV, and DA) was employed to acquire accurate and physically meaningful spectral EM fraction images spanning from 1991 to 2020. The root mean square error (RMSE) for all spectral mixed analysis images was found to be less than 0.01, underscoring the excellent applicability of the LSMA model within our study area [18].

3.2.2. Mapping Coastal Wetland

Random forest (RF) is a powerful ensemble learning method that aggregates multiple decision trees to generate outputs, utilizing the concepts of ensemble learning and random space theory. RF is widely used for tasks such as land cover classification and regression prediction [33,34]. In our study, we set the number of decision trees to 800, considering it as a crucial parameter for the RF model. The other parameters were kept at default values as they are already well-suited for the RF model [27]. We utilized the multi-seasonal spectral EM fraction images we constructed as the input variables for the RF model to map coastal wetlands in the YRD.

During the visual inspection of coastal wetland mapping results [35], some inevitable errors were identified in the automatic classification results of the RF model. For instance, misclassifications occurred between aquaculture and reservoirs, and misclassifications were observed in adjacent areas among different wetlands. To ensure the highest coastal wetland classification accuracy, we corrected these misclassifications by leveraging extensive field data, local expert knowledge, and additional references [12,36]. Additionally, to enhance the robustness of coastal wetland mapping, we employed a majority filter analysis using 5×5 moving windows in the ENVI 5.3.1 software used [37].

3.3. Mapping Accuracy Assessment

The confusion matrix is a widely utilized method for assessing mapping accuracy [28]. In our study, we employed several key metrics for accuracy assessment of coastal wetland mapping: overall accuracy (OA), Kappa coefficient (KC), producer's accuracy (PA), and user's accuracy (UA) [38]. Overall accuracy (OA): this metric represents the ratio of the number of pixels that were correctly classified to the total number of pixels. Kappa coefficient (KC): KC measures the consistency between the classification results and the actual types, providing a valuable assessment of classification quality. Producer's accuracy (PA): PA represents the probability that a verification sample pixel is consistent with the classification result, focusing on the accuracy of the classification process. User's accuracy (UA): UA signifies the ratio of the number of correctly classified pixels to the total number

of pixels assigned to a particular category, indicating the reliability of the classification for specific categories.

3.4. Landscape Indices of Coastal Wetlands

Landscape indices effectively encapsulate a diverse array of information regarding various landscapes, encompassing their structural composition and spatial heterogeneity. In our analysis, we selected eight indices at both the landscape and type levels, namely number of patches (NP) and patch density (PD): reflecting fragmentation levels, where a higher value indicates greater fragmentation. Largest patch index (LPI): indicates the dominance of each landscape. Landscape shape index (LSI): characterizes landscape complexity, with a larger LSI denoting higher complexity. Perimeter–area fractal dimension (PAFRAC): reflects the impact of human activities on landscapes. Shannon’s diversity index (SHDI) and Shannon’s evenness index (SHEI): describe diversity, uniformity, and heterogeneity of each landscape. Aggregation index (AI): reflects the degree of patch aggregation. The calculation of these landscape indices was performed using Fragstats v4.2.1 software.

4. Results

4.1. Accuracy Assessment of Coastal Wetland Mapping

The accuracy of our coastal wetland mapping in the Yellow River Delta (YRD) for the period 1991–2020 demonstrated high precision, with an overall accuracy consistently exceeding 96% (Table S3). Both producer’s and user’s accuracies consistently surpassed 90%, indicating the reliability of our results. The Kappa coefficient, measuring the consistency between classification outcomes and actual types, stood at an impressive 0.96, affirming strong agreement with the sample data. In terms of accuracies related to wetland types, natural coastal wetlands exhibited generally higher producer’s and user’s accuracies compared to human-made wetlands. Human-made wetlands, being more susceptible to human-induced disturbances, showed accuracies ranging from 92% to 99%. Specifically, natural wetland vegetation, including *S. alterniflora*, *P. australis*, and *S. salsa*, displayed slightly higher mapping accuracies than bare flats and wet tidal flats. In the year 2020, the producer’s accuracies for wetland vegetation were consistently around 97%. Notably, the user’s accuracy for *S. salsa* was the highest, reaching 99%, likely attributed to its unique physiological and spectral characteristics in high-salinity environments.

4.2. Coastal Wetland Dynamics during 1991–2020 in the YRD

During 1991–2008, coastal wetlands experienced increased human disturbances, evident from the rise in the PAFRAC, suggesting alterations in their structural complexity (Table S4). This period saw a decline in *P. australis*, *S. salsa*, and bare flat areas of 20.14×10^3 ha, 6.62×10^3 ha, and 38.16×10^3 , respectively (Figure S4). The coastal wetlands suffered fragmentation, as indicated by the elevated NP and PD. The LPI showed a decreasing trend, signifying reduced dominance of coastal wetlands. Furthermore, natural wetlands were transformed into human-made wetlands, arable land, and built-up areas due to local utilization and economic activities. Particularly, 87.78×10^3 ha of tidal flats were converted into built-up areas, aquaculture, and salt exploitation sites, notably in the north and east of the YRD. Over the 30-year span, there was an increase in landscape types and the heterogeneity of coastal wetlands, reflected in the rise of SHDI and SHEI. In 2020, following wetland protection strategies post-2018, natural wetlands were restored, encompassing an area of 12.83×10^3 ha (Figure S4). In 2020, coastal natural wetlands were primarily concentrated in the eastern coastal zone, especially in the YRD estuary, comprising areas occupied by the *S. alterniflora* (5.18×10^3 ha), the *P. australis* (9.62×10^3 ha), the *S. salsa* (9.40×10^3 ha), the bare flat (35.62×10^3 ha), and the wet tidal flat (21.82×10^3 ha). On the other hand, human-made coastal wetlands predominantly existed in the eastern and northern nearshore regions, with a notable increase over the

30-year period. In 2020, 84.30% of these human-made wetlands constituted aquaculture and salt exploitation sites.

4.3. The Evolution Dynamics of Different Wetland Vegetation in the YRD Estuary

The native coastal wetland vegetation in the Yellow River Delta (YRD) primarily comprised the *P. australis* and the *S. salsa*, with areas of 38.88×10^3 ha and 19.08×10^3 ha, respectively (Figure S4). These two native species had distinct distributions based on their growth preferences. The *P. australis* thrived in humid areas near riverbanks and the YRD estuary (Figure 4); however, its area diminished by approximately 29.26×10^3 ha over 30 years, primarily due to encroachment by arable land and the invasive species *S. alterniflora*. On the other hand, the *S. salsa* showed high susceptibility to local environmental conditions, preferring areas with high salinity and humidity, primarily distributed in the eastern coastal region, especially the YRD estuary. However, changes in soil and water conditions led to significant spatial distribution variations in *S. salsa*, with some areas degrading into bare flats (Figure S5). Additionally, parts of the *S. salsa* habitat were overtaken by *S. alterniflora*, particularly in the YRD estuary from 2008 to 2020. During the 30-year period, the largest patch index (LPI) of *S. alterniflora* rapidly increased, while that of *P. australis* decreased (Table S5). The LPI of *S. salsa* fluctuated due to its sensitivity to environmental changes. This suggested that *S. alterniflora* became the dominant invasive species in coastal wetland vegetation, encroaching on the habitat of native species. However, the landscape shape index (LSI) of *P. australis* and *S. salsa* remained significantly higher than that of *S. alterniflora* from 1991 to 2020, indicating greater landscape complexity for the native species.

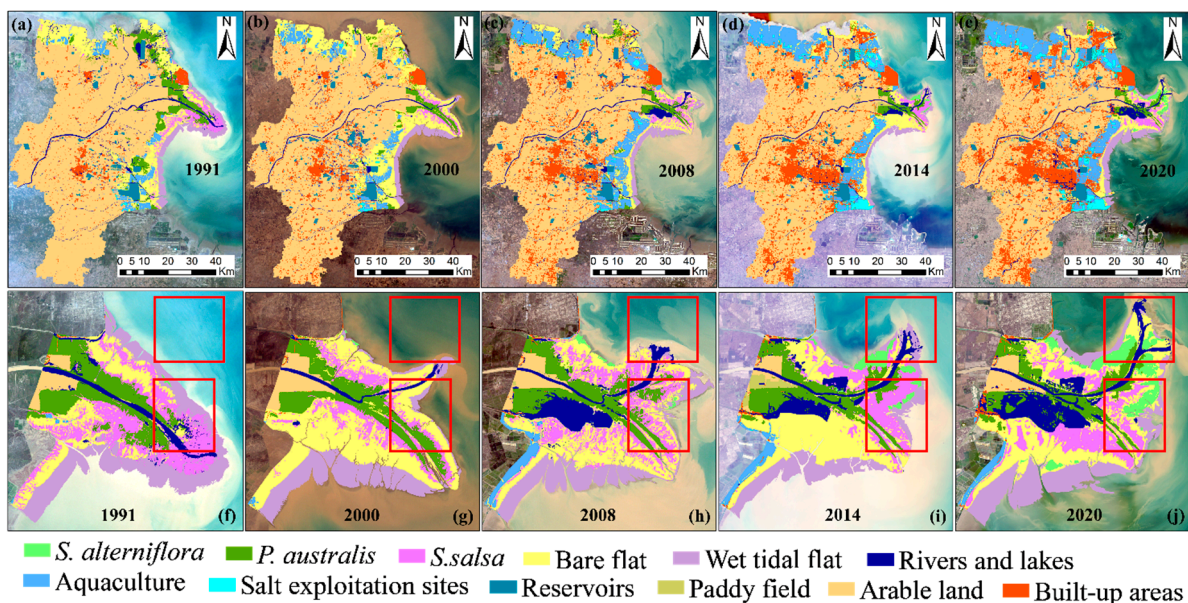


Figure 4. Classification maps of coastal wetlands in the YRD from 1991 to 2020. (a) 1991, (b) 2000, (c) 2008, (d) 2014, (e) 2020, (f) the YRD estuary in 1991, (g) the YRD estuary in 2000, (h) the YRD estuary in 2008, (i) the YRD estuary in 2014, (j) the YRD estuary in 2020.

As an invasive species, the *S. alterniflora* was introduced as a silt-promoting and beach-protecting species in 1990, initially limited to the north bank of the YRD estuary in 1991 (A in Figure 5a), covering an area of 0.16×10^3 ha (Figure S4). Subsequently, its expansion was gradual, primarily occurring in the northern estuary from 1991 to 2008 (A in Figure 5a–c). However, from 2008 onwards, the *S. alterniflora* rapidly expanded in the northern and eastern estuary (B in Figure 5c–e) due to robust reproduction and a lack of natural predators. It also appeared in the southern area of the YRD estuary by 2020 (C in Figure 5e). The increase in its aggregation index (AI) indicated agglomerative expansion (Table S5). Over the 30-year span, the area of *S. alterniflora* expanded more than

30-fold, significantly impacting local coastal wetland biodiversity. Notably, *S. alterniflora* encroached upon 1190.58 ha of *S. salsa* and 72.10 ha of *P. australis* during this period, particularly between 2008 and 2020.

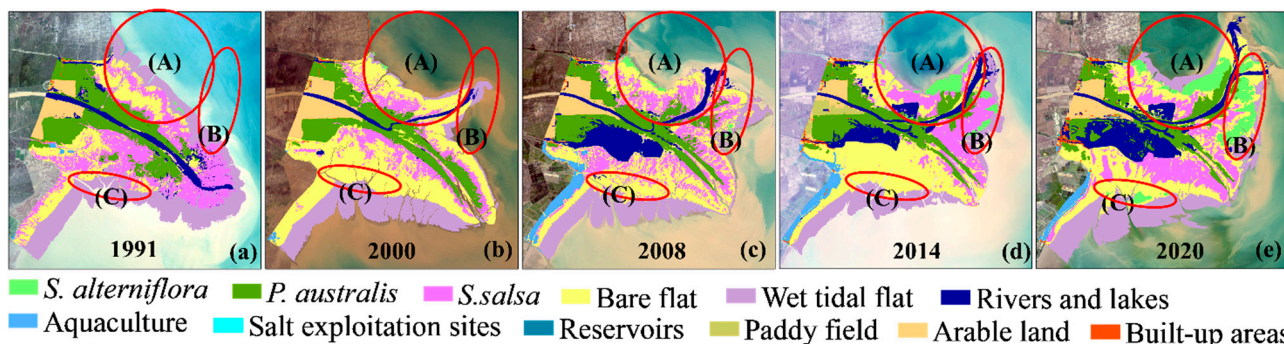


Figure 5. Coastal wetland vegetation in the YRD estuary from 1991 to 2020. (a) 1991, (b) 2000, (c) 2008, (d) 2014, (e) 2020.

4.4. Bare Flat and Human-Made Wetland Dynamics in the YRD

The bare flat, despite providing essential ecosystem services, had limited economic benefits. As a result, it was extensively utilized for aquaculture and salt exploitation in our study area (Figure 4). The bare flat area significantly reduced by about 77.81×10^3 ha in the northern and eastern YRD from 2000 to 2020. Aquaculture experienced a rapid increase from 1991 to 2008 due to high economic benefits and increasing demand for aquatic products. During this period, 75.71% of the expansion was attributed to the conversion of bare flat to aquaculture. The landscape patch index (LPI) of aquaculture showed a continuous increase in both 2014 and 2020, signifying a sustained enhancement of aquaculture dominance (Table S5). By 2020, aquaculture was predominantly concentrated in the eastern and northern parts of our study area. However, the rate of aquaculture expansion significantly declined from 2008 to 2020 due to constraints such as limited water resources, stringent environmental regulations, and aquaculture limitations. Furthermore, the perimeter–area fractal dimension (PAFRAC) increased from 1991 to 2008 and then decreased from 2008 to 2020, indicating a changing extent of disturbance to aquaculture by human activities during these periods.

Salt exploitation sites were another significant human-made wetland in our study area. Initially limited to the southeast coast in 1991, their distribution expanded widely along the northern and eastern coasts by 2020 (Figure 4). Over 30 years, the area of salt exploitation sites increased by 20.15×10^3 ha (Figure S4). The increase in the aggregation index (AI) for salt exploitation sites indicated a higher degree of aggregation compared to previous years (Table S5). Interestingly, during 2008–2020, 13,687.40 ha of aquaculture areas were transformed into salt exploitation sites, while only 3114.33 ha of salt exploitation sites were converted into aquaculture (Figure S5).

5. Discussion

5.1. Comparison with Other Coastal Wetland Results in the YRD

We conducted a comparative analysis with several global and regional datasets to validate the accuracy and consistency of our coastal wetland mapping in the Yellow River Delta (YRD) with the global intertidal change dataset (GIT dataset), the typical salt-marsh vegetation dataset (MTS dataset), and the GlobeLand30.

The GIT dataset was produced at 3-year intervals (<https://www.intertidal.app/download>, accessed on 10 January 2023), covering the 30-year period of 1984–2016 [39]. According to GIT's definition, the intertidal data correspond to tidal flats in our study. We mapped coastal wetlands for the years 1991, 2000, 2008, 2014, and 2020 in our study area, comparing our results with GIT maps for 1990–1992, 1999–2001, 2008–2010, and 2014–2016. The tidal flat area in our YRD dataset for 2008 and 2014 closely matched GIT's

data, showing good spatial alignment (Figure 6a–h). However, our dataset showed more tidal flats in 1991 and 2000 than in the GIT dataset. This discrepancy was mainly due to GIT being a global dataset based on Landsat images using 56 spectral classification variables (such as NDWI and NDVI), while we used fractional images obtained through the LSMA method. Consequently, some areas classified as tidal flats in the GIT dataset, including aquaculture and reservoirs, differed from our classification [16,40]. Nonetheless, our YRD dataset generally exhibited good consistency with the GIT data, despite these differences.

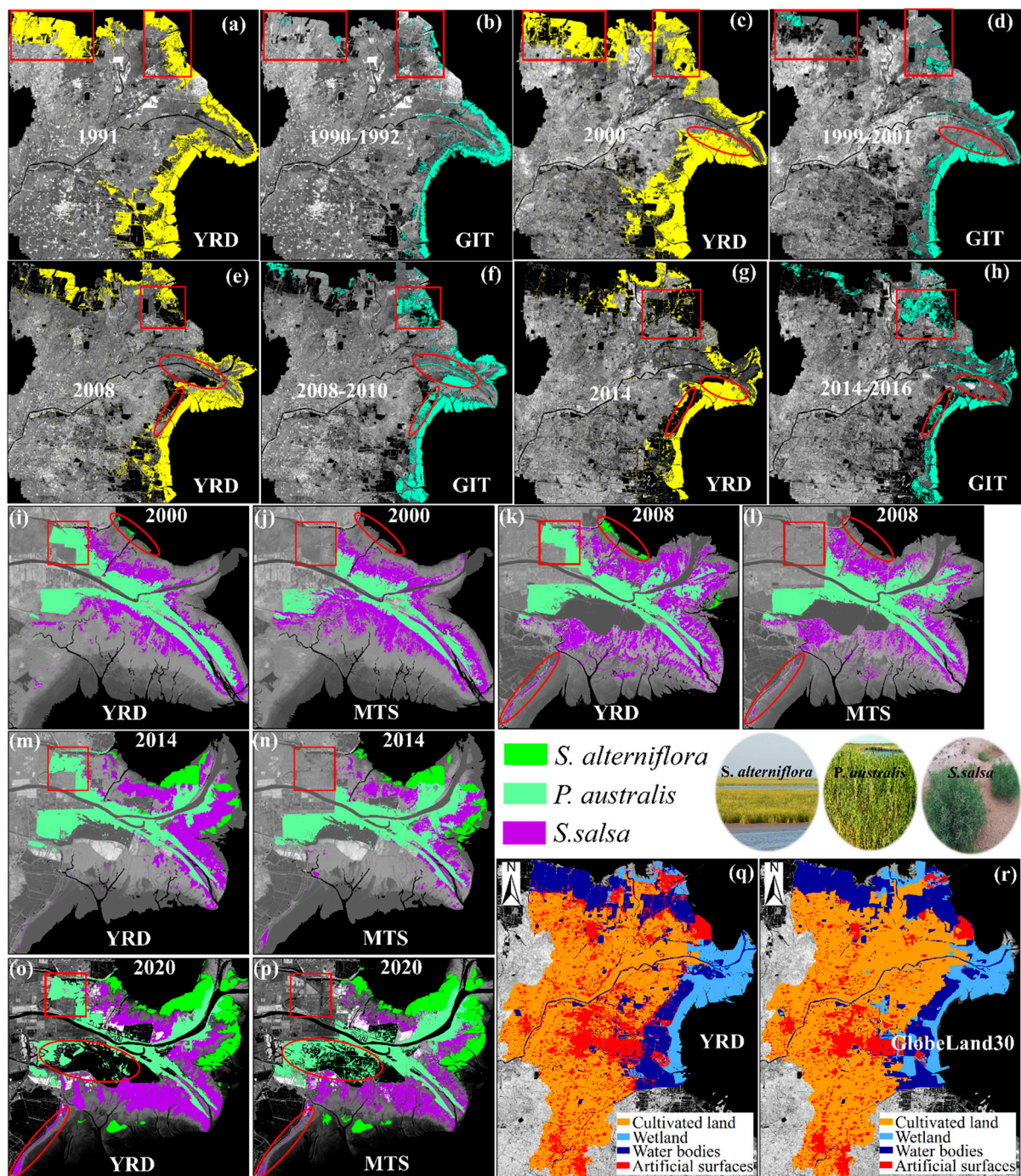


Figure 6. Comparison with other mapping coastal wetlands in the YRD, (a–h) the tidal flats from our YRD dataset and the GIT dataset, (i–p) the *S. alterniflora*, *P. australis* and *S. salsa* from our YRD dataset and the MTS dataset, and (q,r) the YRD dataset and the GlobeLand30 dataset in 2020.

The MTS dataset was produced with the optical data of Landsat TM/ETM/OLI and Sentinel-2 MSI, as well as Sentinel-1 SAR radar data [28]. The three typical salt marsh vegetation types identified in the MTS dataset align with the categories defined in our study, encompassing *S. alterniflora*, *P. australis*, and *S. salsa*. The distribution of *S. alterniflora* in our YRD dataset for 2014 and 2020 closely corresponds with that in the MTS dataset (Figure 6i–p). Wang et al. noted that *S. alterniflora* was introduced to our study area in 1990, and its area measured 66.78 ha in our 2000 study [27]. Interestingly, *S. alterniflora* was absent in the MTS dataset at that time. Moreover, the area covered by *S. alterniflora* (7.47 ha) in the 2008 MTS dataset was smaller than in our dataset (407.61 ha). While the *P. australis* areas in the YRD and MTS datasets for 2008 and 2014 showed a good match, our *P. australis* area was 2938.27 ha larger than the MTS dataset for 2000, particularly in the northwest of our study area. Additionally, the MTS dataset indicated approximately 1574.03 ha more *P. australis* than our result for 2020, though the spatial distribution of *S. salsa* was generally consistent in both datasets. These discrepancies could be attributed to variations in remote sensing imagery, resolutions, and classification variables between the two datasets [41].

We compared our results in the Yellow River Delta (YRD) with the classification system based on GlobeLand30 (<http://www.globallandcover.com/>, accessed on 10 January 2023) (Table S6). The wetland area in our study exhibited high consistency with GlobeLand30 in 2020, and the spatial distribution also matched well (Figure 6q,r). However, there were discrepancies between these two datasets due to variations in remote sensing images and classification methods [21]. Specifically, the cultivated land area in the GlobeLand30 dataset exceeded our result by 45,236.25 ha, while the artificial surfaces were 51,219.99 ha less in the GlobeLand30 dataset. Furthermore, the water bodies' area in the GlobeLand30 dataset was 10,715.67 ha smaller than that in our YRD dataset. In terms of overall accuracy (OA) and Kappa coefficient (KC), the GlobeLand30 dataset for 2020 reported an OA of 85.72% and a KC of 0.82. In comparison, our 2020 coastal wetland mapping achieved a higher OA of 97.30% and a higher KC of 0.97, emphasizing the accuracy and precision of our mapping approach.

5.2. The Impacts of Coastal Wetland Dynamics in the YRD Area

Over the past 30 years, the extensive spread of *S. alterniflora* brought about adverse effects. For instance, *S. alterniflora* alters the flow patterns and trajectories of water bodies, leading to shifts in local sediment dynamics within the YRD estuary. This, in turn, modified the evolution of the local estuary, posing a threat to the coastal environment [10]. Additionally, *S. alterniflora* encroached upon the natural habitats of native species such as *P. australis* and *S. salsa* due to its favorable environment and lack of natural predators. Consequently, this invasion resulted in significant losses in biodiversity within our study area [10]. Various strategies and measures, such as physical removal, chemical treatment, and biological control, were implemented to curb the further invasion of *S. alterniflora* [10,42]. Our study, by providing a detailed analysis of the dynamics of different wetland vegetation, can play a critical role in monitoring the invasion of *S. alterniflora* and issuing early warnings.

Apart from invasive species, human activities also contributed to the depletion of natural coastal wetlands [16]. Wu et al. highlighted that the expansion of coastal construction resulted in the loss and fragmentation of natural wetlands in China, elevating the risk of coastal disasters such as storm surges and tsunamis [43]. Oil exploitation further encroached upon natural coastal wetlands, such as *P. australis* in the YRD, causing degradation and secondary salinization [44]. Furthermore, cropland cultivation, often accompanied by excessive water usage, accelerated the degradation of natural wetlands due to water scarcity, especially affecting wetland vegetation such as *P. australis* [44].

In a study by Wang et al., aquaculture was identified as the primary cause of tidal flat loss in the YRD, contributing to significant environmental challenges [10]. Excessive use of aquaculture facilities such as fences and cages led to wetland reduction and water pollution [45]. Intensive aquaculture practices, including high-density breeding, over-feeding, and excessive chemical usage, resulted in substantial nitrogen and phosphorus

accumulation in the local watershed and soil, posing a high risk of eutrophication and environmental contamination [11]. Therefore, improving aquaculture efficiency and developing environmentally sustainable aquaculture systems are of paramount importance [43]. However, it is critical to strike a balance between local economic development and wetland protection, as aquaculture yielded substantial economic gains at the cost of natural wetlands [46]. Hence, a detailed monitoring of coastal wetland dynamics can provide valuable insights to navigate the trade-offs between different coastal wetland management, protection, and utilization strategies.

5.3. Advantage, Limitation and Future Study

Previous studies primarily focused on fine-classifying coastal wetlands based on differences in band spectral indices [47]. For instance, Yin et al. mapped *S. salsa* from 1990 to 2020 in the Bohai Bay using spectral indices and a decision tree algorithm applied to Landsat images [41]. Zhang et al. mapped typical salt marsh species in the YRD utilizing temporal–spatial–spectral multidimensional features [28]. However, these studies were largely specific to certain wetlands and did not consider the broader spectrum of coastal wetlands and their dynamics. This is due to the challenge of exploring complex coastal wetlands with similar spectral information, particularly achieving fine classification amidst high spatiotemporal heterogeneity [48,49].

In our study, we established four standard spectral endmembers (EMs) of SL, SA, GV, and DA in the YRD. The LSMA method enabled the transformation of original spectral images into fractional values in the standard EM spectral space, enhancing the interpretability and understanding of the spectrum [19]. Multi-seasonal GV effectively differentiates wetland vegetation from other types, facilitating the accurate distinction of wetland vegetation (such as *P. australis*) with similar spectral characteristics [50]. Additionally, SA rapidly identifies salt exploitation sites with highly fractional values [18]. The fractional proportions of different EMs also aid in distinguishing aquaculture from other coastal wetlands (such as rivers and lakes).

However, there are certain limitations in our study. Due to restricted samples and remote sensing image availability, there were some misclassifications in coastal wetland mapping. The spatial resolution limitation (30 m) led to the merging of small patches, such as *P. australis* and *S. salsa*. To address this, future research could optimize samples and integrate higher-resolution satellite images (e.g., Sentinel-2) to obtain more detailed spectral information and enhance the accuracy of coastal wetland mapping. Tidal flats, being highly complex due to tidal and climatic influences, present another challenge. Future endeavors could incorporate additional auxiliary data such as climate and tides to further enhance the accuracy of tidal flat mapping. Moreover, our study did not conduct quantitative analyses on the drivers of coastal wetland dynamics and changes in ecosystem services. Future work could leverage detailed socioeconomic data to investigate these intriguing questions.

6. Conclusions

Detailed classification of coastal wetlands is crucial for local sustainable development and wetland protection. Despite some limitations, our study successfully mapped coastal wetland changes and conducted dynamic analysis from 1991 to 2020 using the LSMA method. The accuracy of our coastal wetland mapping in the YRD was high, with an overall accuracy exceeding 96%. Notably, the YRD estuary saw significant expansion of approximately 8744.58 ha to the east and north during 1991–2020, resulting in substantial spatial morphology changes.

During 1991–2008, numerous natural wetlands transitioned into human-made wetlands such as aquaculture, arable land, and built-up areas. However, after 2014, some natural wetlands underwent restoration. The invasion of the invasive species *S. alterniflora* significantly impacted two forms of native wetland vegetation, *P. australis* and *S. salsa*, with substantial encroachment during 2008–2020. *S. alterniflora* expanded rapidly during this period, advancing about 5 km off the coast over three decades.

The transformation of bare flat areas into aquaculture and salt exploitation sites was notable due to their high economic value. Despite different methodologies and remote sensing data, our mapping results are highly consistent with previous findings from the GIT dataset, the MTS dataset, and the GlobeLand30. Coastal wetland dynamics have significant impacts on local ecosystem services, including fragmented natural coastal wetlands, reduced biodiversity, and environmental pollution, even though some human-made wetlands generated economic benefits. Balancing the protection of natural wetlands with local social development is a crucial consideration for the future.

Supplementary Materials: The following supporting information can be downloaded at: <https://www.mdpi.com/article/10.3390/rs15205003/s1>, Figure S1: Eigenvalues ordered highest to zero, and cumulative PC variance (%). The cumulative variance of the three primary PCs (PC1 to PC3), was greater than 98%, meaning nearly all the image parameter information can be represented by these PCs; Figure S2: Scatter plot for TM endmember spectral extraction; Figure S3: Scatter plot for OLI endmember spectral extraction; Figure S4: Area and proportion of coastal wetlands in the YRD from 1991 to 2020; Figure S5: The transitions of coastal wetlands in the YRD from 1991 to 2020; Table S1: List of remote sensing image data; Table S2: Training and validation samples (pixels) for coastal wetlands during the period of 1991–2020; Table S3: Accuracy assessment of coastal wetlands classification during the period of 1991–2020; Table S4: Landscape-level indices for coastal wetlands during the period of 1991–2020; Table S5: Class-level indices for coastal wetlands during the period of 1991–2020; Table S6: Classification system based on GlobeLand30 for comparison.

Author Contributions: Conceptualization K.T., F.L. and D.S.; methodology: K.T.; software: K.T. and F.L.; formal analysis: W.D., B.W., Q.S., X.L., H.Z. and Y.L.; data curation, K.T. and B.W.; writing—original draft: K.T., F.L. and D.S.; writing—review and editing: all authors. All authors have read and agreed to the published version of the manuscript.

Funding: This work is supported by the National Natural Science Foundation of China (41801202) and the Key Laboratory of Southeast Coast Marine Information Intelligent Perception and Application, MNR, China (220104).

Data Availability Statement: The data presented in this study are available on request from the corresponding author. The data are not publicly available due to privacy.

Conflicts of Interest: The authors declare no conflict of interest.

References

1. Kou, W.; Dong, J.; Xiao, X.; Hernandez, A.J.; Qin, Y.; Zhang, G.; Chen, B.; Lu, N.; Doughty, R. Expansion dynamics of deciduous rubber plantations in Xishuangbanna, China during 2000–2010. *GISci. Remote Sens.* **2018**, *55*, 905–925. [[CrossRef](#)]
2. Costanza, R.; D’Arge, R.; De Groot, R.; Farber, S.; Grasso, M.; Hannon, B.; Limburg, K.; Naeem, S.; O’Neill, R.V.; Paruelo, J.; et al. The value of the world’s ecosystem services and natural capital. *Nature* **1997**, *387*, 253–260. [[CrossRef](#)]
3. Ericson, J.P.; Vörösmarty, C.J.; Dingman, S.L.; Ward, L.G.; Meybeck, M. Effective sea-level rise and deltas: Causes of change and human dimension implications. *Glob. Planet. Chang.* **2006**, *50*, 63–82. [[CrossRef](#)]
4. Liu, Y.; Li, J.; Sun, C.; Wang, X.; Tian, P.; Chen, L.; Zhang, H.; Yang, X.; He, G. Thirty-year changes of the coastlines, wetlands, and ecosystem services in the Asia major deltas. *J. Environ. Manag.* **2023**, *326*, 116675. [[CrossRef](#)]
5. Schuerch, M.; Spencer, T.; Temmerman, S.; Kirwan, M.L.; Wolff, C.; Lincke, D.; McOwen, C.J.; Pickering, M.D.; Reef, R.; Vafeidis, A.T.; et al. Author correction: Future response of global coastal wetlands to sea-level rise. *Nature* **2019**, *569*, E8. [[CrossRef](#)]
6. Morris, J.T.; Sundareshwar, P.V.; Nietch, C.T.; Kjerfve, B.; Cahoon, D.R. Responses of coastal wetlands to rising sea level. *Ecology* **2002**, *83*, 2869–2877. [[CrossRef](#)]
7. MacAlister, C.; Mahaxay, M. Mapping wetlands in the lower Mekong Basin for wetland resource and conservation management using Landsat ETM images and field survey data. *J. Environ. Manag.* **2009**, *90*, 2130–2137. [[CrossRef](#)] [[PubMed](#)]
8. Thorne, K.; MacDonald, G.; Guntenspergen, G.; Ambrose, R.; Buffington, K.; Dugger, B.; Freeman, C.; Janousek, C.; Brown, L.; Rosencranz, J.; et al. US Pacific coastal wetland resilience and vulnerability to sea-level rise. *Sci. Adv.* **2018**, *4*, eaao3270. [[CrossRef](#)]
9. Wang, B.; Zhang, K.; Liu, Q.; He, Q.; van de Koppel, J.; Teng, S.N.; Miao, X.; Liu, M.; Bertness, M.; Xu, C. Long-distance facilitation of coastal ecosystem structure and resilience. *Proc. Natl. Acad. Sci. USA* **2022**, *119*, e2123274119. [[CrossRef](#)]
10. Wang, X.; Xiao, X.; Xu, X.; Zou, Z.; Chen, B.; Qin, Y.; Zhang, X.; Dong, J.; Liu, D.; Pan, L.; et al. Rebound in China’s coastal wetlands following conservation and restoration. *Nat. Sustain.* **2021**, *4*, 1076–1083. [[CrossRef](#)]
11. Duan, Y.; Tian, B.; Li, X.; Liu, D.; Sengupta, D.; Wang, Y.; Peng, Y. Tracking changes in aquaculture ponds on the China coast using 30 years of landsat images. *Int. J. Appl. Earth Obs. Geoinf.* **2021**, *102*, 102383. [[CrossRef](#)]

12. Mao, D.; Wang, Z.; Du, B.; Li, L.; Tian, Y.; Jia, M.; Zeng, Y.; Song, K.; Jiang, M.; Wang, Y. National wetland mapping in China: A new product resulting from object-based and hierarchical classification of Landsat 8 OLI images. *ISPRS J. Photogramm. Remote Sens.* **2020**, *164*, 11–25. [[CrossRef](#)]
13. Ghosh, S.; Mishra, D.R.; Gitelson, A.A. Long-term monitoring of biophysical characteristics of tidal wetlands in the northern Gulf of Mexico—A methodological approach using MODIS. *Remote Sens. Environ.* **2016**, *173*, 39–58. [[CrossRef](#)]
14. Jin, H.; Huang, C.; Lang, M.W.; Yeo, I.-Y.; Stehman, S.V. Monitoring of wetland inundation dynamics in the Delmarva Peninsula using Landsat time-series imagery from 1985 to 2011. *Remote Sens. Environ.* **2017**, *190*, 26–41. [[CrossRef](#)]
15. Zhu, Z.; Wulder, M.A.; Roy, D.P.; Woodcock, C.E.; Hansen, M.C.; Radeloff, V.C.; Healey, S.P.; Schaaf, C.; Hostert, P.; Strobl, P.; et al. Benefits of the free and open Landsat data policy. *Remote Sens. Environ.* **2019**, *224*, 382–385. [[CrossRef](#)]
16. Wang, X.; Xiao, X.; Zou, Z.; Hou, L.; Qin, Y.; Dong, J.; Doughty, R.B.; Chen, B.; Zhang, X.; Chen, Y.; et al. Mapping coastal wetlands of China using time series Landsat images in 2018 and Google Earth Engine. *ISPRS J. Photogramm. Remote Sens.* **2020**, *163*, 312–326. [[CrossRef](#)]
17. Sun, S.; Zhang, Y.; Song, Z.; Chen, B.; Zhang, Y.; Yuan, W.; Chen, C.; Chen, W.; Ran, X.; Wang, Y. Mapping coastal wetlands of the Bohai Rim at a spatial resolution of 10 m using multiple open-access satellite data and terrain indices. *Remote Sens.* **2020**, *12*, 4114. [[CrossRef](#)]
18. Sun, D.; Liu, N. Coupling spectral unmixing and multiseasonal remote sensing for temperate dryland land-use/land-cover mapping in Minqin County, China. *Int. J. Remote Sens.* **2015**, *36*, 3636–3658. [[CrossRef](#)]
19. Sun, D.; Zhang, P.; Sun, Q.; Jiang, W. A dryland cover state mapping using catastrophe model in a spectral endmember space of OLI, a case study in Minqin, China. *Int. J. Rem. Sens.* **2019**, *40*, 5673–5694. [[CrossRef](#)]
20. Sun, Q.; Zhang, P.; Jiao, X.; Han, W.; Sun, Y.; Sun, D. Identifying and understanding alternative states of dryland landscape: A hierarchical analysis of time series of fractional vegetation-soil nexuses in China’s Hexi Corridor. *Landsc. Urban Plans.* **2021**, *215*, 104225. [[CrossRef](#)]
21. Chen, B.; Xiao, X.; Li, X.; Pan, L.; Doughty, R.; Ma, J.; Dong, J.; Qin, Y.; Zhao, B.; Wu, Z.; et al. A mangrove forest map of China in 2015: Analysis of time series Landsat 7/8 and Sentinel-1A imagery in Google Earth Engine cloud computing platform. *ISPRS J. Photogramm. Remote Sens.* **2017**, *131*, 104–120. [[CrossRef](#)]
22. Wang, X.; Xiao, X.; Zou, Z.; Chen, B.; Ma, J.; Dong, J.; Doughty, R.B.; Zhong, Q.; Qin, Y.; Dai, S.; et al. Tracking annual changes of coastal tidal flats in China during 1986–2016 through analyses of Landsat images with Google Earth Engine. *Remote Sens. Environ.* **2018**, *238*, 110987. [[CrossRef](#)] [[PubMed](#)]
23. Ding, X.; Shan, X.; Chen, Y.; Jin, X.; Muhammed, F.R. Dynamics of shoreline and land reclamation from 1985 to 2015 in the Bohai Sea, China. *J. Geogr. Sci.* **2020**, *29*, 2031–2046. [[CrossRef](#)]
24. Ning, Z.; Li, D.; Chen, C.; Xie, C.; Chen, G.; Xie, T.; Wang, Q.; Bai, J.; Cui, B. The importance of structural and functional characteristics of tidal channels to smooth cordgrass invasion in the Yellow River Delta, China: Implications for coastal wetland management. *J. Environ. Manag.* **2023**, *342*, 118297. [[CrossRef](#)] [[PubMed](#)]
25. Jiao, L.; Sun, W.; Yang, G.; Ren, G.; Liu, Y. A hierarchical classification framework of satellite multispectral/hyperspectral images for mapping coastal wetlands. *Remote Sens.* **2019**, *11*, 2238. [[CrossRef](#)]
26. Liu, C.; Tao, R.; Li, W.; Zhang, M.; Sun, W.; Du, Q. Joint classification of hyperspectral and multispectral images for mapping coastal wetlands. *IEEE J. Sel. Top. Appl. Earth Obs. Remote Sens.* **2021**, *14*, 982–996. [[CrossRef](#)]
27. Wang, Z.; Ke, Y.; Chen, M.; Zhou, D.; Zhu, L.; Bai, J. Mapping coastal wetlands in the Yellow River Delta, China during 2008–2019: Impacts of valid observations, harmonic regression, and critical months. *Int. J. Remote Sens.* **2021**, *42*, 7880–7906. [[CrossRef](#)]
28. Zhang, C.; Gong, Z.; Qiu, H.; Zhang, Y.; Zhou, D. Mapping typical salt-marsh species in the Yellow River Delta wetland supported by temporal-spatial-spectral multidimensional features. *Sci. Total Environ.* **2021**, *783*, 147061. [[CrossRef](#)]
29. GB/T 24708-2009; Wetland Classification. National Forestry and Grassland Administration: Beijing, China, 2009.
30. Van der Meer, F.D.; Jia, X. Collinearity and orthogonality of endmembers in linear spectral unmixing. *Int. J. Appl. Earth Obs. Geoinf.* **2012**, *18*, 491–503. [[CrossRef](#)]
31. Small, C. The Landsat ETM+ spectral mixing space. *Remote Sens. Environ.* **2004**, *93*, 1–17. [[CrossRef](#)]
32. Somers, B.; Asner, G.P.; Tits, L.; Coppin, P. Endmember variability in spectral mixture analysis: A review. *Remote Sens. Environ.* **2011**, *115*, 1603–1616. [[CrossRef](#)]
33. Breiman, L. Random Forests. *Mach. Learn.* **2001**, *45*, 5–32. [[CrossRef](#)]
34. Palmer, D.S.; O’Boyle, N.M.; Glen, R.C.; Mitchell, J.B. Random forest models to predict aqueous solubility. *J. Chem. Inf. Model.* **2007**, *47*, 150–158. [[CrossRef](#)]
35. Li, Y.; Niu, Z. Systematic method for mapping fine-resolution water cover types in China based on time series Sentinel-1 and 2 Images. *Int. J. Appl. Earth Obs. Geoinf.* **2022**, *106*, 102656. [[CrossRef](#)]
36. Liu, Y.; Zhang, H.; Zhang, M.; Cui, Z.; Lei, K.; Zhang, J.; Yang, T.; Ji, P. Vietnam wetland cover map: Using hydro-periods Sentinel-2 images and Google Earth Engine to explore the mapping method of tropical wetland. *Int. J. Appl. Earth Obs. Geoinf.* **2022**, *115*, 103122. [[CrossRef](#)]
37. McCarthy, M.J.; Radabaugh, K.R.; Moyer, R.P.; Muller-Karger, F.E. Enabling efficient, large-scale high-spatial resolution wetland mapping using satellites. *Remote Sens. Environ.* **2018**, *208*, 189–201. [[CrossRef](#)]
38. Pontius, R.G.; Millones, M. Death to Kappa: Birth of quantity disagreement and allocation disagreement for accuracy assessment. *Int. J. Remote Sens.* **2011**, *32*, 4407–4429. [[CrossRef](#)]

39. Murray, N.J.; Phinn, S.R.; DeWitt, M.; Ferrari, R.; Johnston, R.; Lyons, M.B.; Clinton, N.; Thau, D.; Fuller, R.A. The global distribution and trajectory of tidal flats. *Nature* **2019**, *565*, 222. [[CrossRef](#)]
40. Ren, C.; Wang, Z.; Zhang, Y.; Zhang, B.; Chen, L.; Xi, Y.; Xiao, X.; Doughty, R.B.; Liu, M.; Jia, M.; et al. Rapid expansion of coastal aquaculture ponds in China from Landsat observations during 1984–2016. *Int. J. Appl. Earth Obs. Geoinf.* **2019**, *82*, 101902. [[CrossRef](#)]
41. Yin, H.; Hu, Y.; Liu, M.; Li, C.; Chang, Y. Evolutions of 30-year spatio-temporal distribution and influencing factors of *Suaeda salsa* in Bohai Bay, China. *Remote Sens.* **2022**, *14*, 138. [[CrossRef](#)]
42. Zhang, X.; Xiao, X.; Wang, X.; Xu, X.; Chen, B.; Wang, J.; Ma, J.; Zhao, B.; Li, B. Quantifying expansion and removal of *Spartina alterniflora* on Chongming island, China, using time series Landsat images during 1995–2018. *Remote Sens. Environ.* **2020**, *247*, 111916. [[CrossRef](#)]
43. Wu, W.; Zhi, C.; Gao, Y.; Chen, C.; Chen, Z.; Su, H.; Lu, W.; Tian, B. Increasing fragmentation and squeezing of coastal wetlands: Status, drivers, and sustainable protection from the perspective of remote sensing. *Sci. Total Environ.* **2022**, *811*, 152339. [[CrossRef](#)] [[PubMed](#)]
44. Peng, J.; Liu, S.; Lu, W.; Liu, M.; Feng, S.; Cong, P. Continuous change mapping to understand wetland quantity and quality evolution and driving forces: A case study in the Liao river estuary from 1986 to 2018. *Remote Sens.* **2021**, *13*, 4900. [[CrossRef](#)]
45. Yang, P.; Lai, D.Y.F.; Jin, B.; Bastviken, D.; Tan, L.; Tong, C. Dynamics of dissolved nutrients in the aquaculture shrimp ponds of the Min River estuary, China: Concentrations, fluxes and environmental loads. *Sci. Total Environ.* **2017**, *603–604*, 256–267. [[CrossRef](#)] [[PubMed](#)]
46. Barbier, E.B.; Koch, E.W.; Silliman, B.R.; Hacker, S.D.; Wolanski, E.; Primavera, J.; Granek, E.F.; Polasky, S.; Aswani, S.; Cramer, L.A.; et al. Coastal ecosystem-based management with nonlinear ecological functions and values. *Science* **2008**, *319*, 321–323. [[CrossRef](#)]
47. Dong, Z.; Wang, Z.; Liu, D.; Song, K.; Li, L.; Jia, M.; Ding, Z. Mapping wetland areas using landsat-derived NDVI and LSWI: A case study of west Songnen Plain, Northeast China. *J. Indian Soc. Remote Sens.* **2014**, *42*, 569–576. [[CrossRef](#)]
48. Su, H.; Yao, W.; Wu, Z.; Zheng, P.; Du, Q. Kernel low-rank representation with elastic net for China coastal wetland land cover classification using GF-5 hyperspectral imagery. *ISPRS J. Photogramm. Remote Sens.* **2021**, *171*, 238–252. [[CrossRef](#)]
49. Sun, W.; Liu, K.; Ren, G.; Liu, W.; Yang, G.; Meng, X.; Peng, J. A simple and effective spectral-spatial method for mapping large-scale coastal wetlands using China ZY1-02D satellite hyperspectral images. *Int. J. Appl. Earth Obs. Geoinf.* **2021**, *104*, 102572. [[CrossRef](#)]
50. McCarthy, M.J.; Merton, E.J.; Muller-Karger, F.E. Improved coastal wetland mapping using very-high 2-meter spatial resolution imagery. *Int. J. Appl. Earth Obs. Geoinf.* **2015**, *40*, 11–18. [[CrossRef](#)]

Disclaimer/Publisher’s Note: The statements, opinions and data contained in all publications are solely those of the individual author(s) and contributor(s) and not of MDPI and/or the editor(s). MDPI and/or the editor(s) disclaim responsibility for any injury to people or property resulting from any ideas, methods, instructions or products referred to in the content.